Experimental observations of the three-dimensional wake structures and dynamics generated by a rigid, bioinspired pitching panel

Justin T. King, Rajeev Kumar, and Melissa A. Green

Phys. Rev. Fluids **3**, 034701 — Published 14 March 2018

DOI: 10.1103/PhysRevFluids.3.034701

Experimental observations of the three-dimensional wake structures and dynamics generated by a rigid, bio-inspired pitching panel

Justin T. King*, Rajeev Kumar, and Melissa A. Green
Mechanical and Aerospace Engineering, Syracuse University, Syracuse, NY, 13244, USA
(Dated: February 7, 2018)

The effects of changing Strouhal number on the three-dimensional wake produced by a rigid, bio-inspired trapezoidal pitching panel are analyzed through the use of stereoscopic particle image velocimetry over a Strouhal number range of 0.17-0.56. The results show that for all cases, at least some section of the wake comprises an alternating series of interacting vortex rings. The behavior of the flows induced by these vortex rings is consistent with the wake phenomena of spanwise compression and transverse expansion. Increases in Strouhal number correspond to an increased rate of spanwise compression, a greater amount of transverse expansion, and the movement of the location of wake breakdown onset upstream.

I. INTRODUCTION

Through over 500 million years of evolution, fish and other aquatic animals have developed the ability to exploit the fluid flows around them via the movements of their bodies, fins, and flukes [1]. As a result, natural selection has generated a variety of fish and cetacean species that are capable of performing fast movements and swimming with a low cost of motion [2]. The fin, fluke, and body motions of these species can create highly three-dimensional, unsteady flow fields that are often comprised of coherent vortex structures that are shed from the trailing and spanwise edges of a fluke or fin.

Measurements of thrust and efficiency have demonstrated that oscillating propulsors can achieve propulsive efficiencies that exceed those of a typical screw propeller system. Anderson *et al.* measured propulsive efficiencies as high as 87% in experiments on a harmonically oscillating airfoil [3]. Yamaguchi and Bose used viscous, nonlinear theory to predict the propulsive efficiencies of rigid and partly flexible oscillating propulsors in open water and behind a ship. Results showed that the open water propulsive efficiencies of the propulsors were 17-25% higher than an optimal screw propeller at their respective design conditions, and that a partly flexible foil placed behind a ship had a quasi-propulsive efficiency approximately 5% higher than a screw propeller [4].

Previous studies have revealed that a relationship exists between the wake structure and the thrust performance of an oscillating foil [3, 5–10]. However, this notion has been recently challenged by Mackowski and Williamson, who found little correlation between thrust coefficient and the arrangement of vortices in the wake of an oscillating airfoil [11]. In that work, the authors viewed wake vortices as vestiges of force generation, rather than drivers of propulsive force. Triantafyllou *et al.* proposed that efficient thrust generation by oscillating foils is related to the formation of a wake with a staggered array of vortices resembling a von Kármán vortex street, but with vortices of a reversed rotational direction [5]. In a reverse von Kármán street, vortices are arranged so that they induce a velocity in the direction of the mean flow, which indicates thrust production under certain conditions. A linear stability analysis demonstrated that thrust production was most efficient within a narrow range of oscillation frequencies. Outside of this frequency range, different wake patterns were observed, including wakes consistent with drag production and inefficient thrust production. The existence of preferred oscillation frequencies for optimal thrust production suggested that the Strouhal number, St, was one of the principal non-dimensional parameters that governed propulsive efficiency. The Strouhal number is a non-dimensional frequency defined as $St = fA/U$, where A is the wake width, f is the frequency of vortex shedding, and U is the freestream speed. The current work focuses on a trapezoidal panel that was pitched about its leading edge. Accordingly, A is approximated as the peak-to-peak trailing edge excursion and f is the pitching frequency. The thrust production and wake behavior of an oscillating foil have also been discussed in terms of the reduced frequency [9, 12]. However, Triantafyllou *et al.* state that St is a more influential governing parameter than reduced frequency, due in part to the ability of St to predict thrust for heaving and pitching foils [13]. Triantafyllou *et al.* predicted that the maximum propulsive efficiency of an oscillating foil would lie within the range $0.25 \leq St \leq 0.35$, and experimental results showed that optimal efficiency occurred within this St range. These experimental results agree well with *in situ* measurements of swimming fish and cetaceans, which showed that certain animals swim within the range $0.2 \leq St \leq 0.4$ [5].

Variation of actuation amplitude or frequency for finite aspect ratio panels has been found to produce a variety of wake patterns, only some of which take the shape of a reverse von Kármán vortex street. The details of these three-dimensional wake patterns are not yet fully understood, but may be crucial to explaining the propulsive efficiencies of oscillating propulsors. Two commonly observed wake patterns are the 2S and 2P wakes, which in-

* Email for correspondence: jtking@syr.edu

volve the shedding of counter-rotating vortices from the trailing edge of a panel or foil during a pitching cycle. In a 2S wake, two single vortices are shed per pitching cycle, with one vortex being shed during each half cycle. In a 2P wake, two pairs of vortices are shed during a pitching cycle, with one pair being shed during each half cycle. A detailed study of the 2S, 2P, and other wake regimes was carried out by Williamson and Roshko, who analyzed the wake created by a circular cylinder oscillating laterally in a freestream flow [14]. 2S and 2P wakes were also observed by Koochesfahani in his study of the vortical patterns found in the wake of a foil pitched at small amplitudes [9]. Other experiments also report upon the development of 2S, 2P, and additional wakes for a pitching foil or panel [15–18].

Experiments on the pitching and heaving of finite aspect ratio bodies have investigated the complex, three-dimensional wakes that they produce. The aspect ratio, AR, of a body is defined in the present work as $AR = b^2/S$, where b is the maximum value of the tip-to-tip span and S is the planform area of the body. von Ellenrieder *et al.* used flow visualization to capture the three-dimensional vortex structures in the wake of a wing experiencing heaving and pitching at a low Reynolds number [19]. Buchholz *et al.* pitched a rigid, rectangular panel about its leading edge at $St = 0.23$, and observed a wake comprised of horseshoe vortices of alternating sign that formed a three-dimensional reverse von Kármán vortex street [20]. They proposed a vortex model for the wake with the streamwise component of vorticity playing a dominant role in the wake dynamics. Two component particle image velocimetry (PIV) and Lagrangian coherent structures were used by Green *et al.* to study the three-dimensional wake of a pitching trapezoidal panel, and the effects of St on wake breakdown and spanwise compression of the wake were noted [15].

Changes in trailing edge geometry have also been shown to influence wake structure and propulsive performance. For pitching rectangular panels with fixed AR, changing the trailing edge from a concave to convex shape was show to increase the coefficient of thrust and propulsive efficiency [21]. However, Buchholz *et al.* were unable to demonstrate a clear relationship between AR and propulsive efficiency for a pitching rectangular panel with a straight trailing edge [22]. Feilich and Lauder showed that the trailing edge and planform shapes of a heaving foil affect performance, but they were unable to establish a predictive relationship between performance and shape [23]. Lee *et al.* investigated the wake structure and performance of rectangular, trapezoidal, and cropped delta shaped foils. They showed that the hydromechanical efficiency of a flapping foil executing start up motions from rest increases as AR increases, while thrust is maximized at a relatively low value of $AR \approx 0.7$ [24].

While not of primary interest in the present work, the inclusion of a heaving motion has also been shown to affect wake structure and performance. In fact, a pure pitching motion was found to be relatively inefficient by Mackowski and Williamson through experiments on a NACA-0012 airfoil [11]. Anderson *et al.* also found that airfoils experiencing heave and pitch performed better than a purely pitching airfoil. Optimal thrust production was found to occur for large heave amplitudes with the phase angle of pitching leading that of heaving by about 75° [3]. Similar results were obtained by Quinn for a rectangular, flexible foil that was pitched and heaved. Within a large parameter space, it was found that propulsive efficiency was globally optimized for large heave-to-chord ratios with a 90° phase offset between pitch and heave [25]. The dynamics and structures of the wake produced by plates rotated and translated in a fluid at rest have also been reported in the literature [26, 27].

Computational studies have been used to examine the wake structures and performance of finite aspect ratio bodies. Guglielmini *et al.* used numerical simulations to model the vortex structures shed by a two-dimensional plate undergoing heave and pitch motions [28]. They quantified the thrust developed, and analyzed the role of vortex structures in the wake. A numerical investigation was performed by Blondeaux *et al* on a finite span foil with prescribed pitch and heave motions [29]. Vortex rings were shown to be shed from the foil every half cycle, with vortex ring dynamics being dependent on St. At relatively low St, interactions between adjacent vortex rings were found to be somewhat weak. A coupled fluid-structure interaction simulation was used by Zhu and Shoele to study the performance of a caudal fin with embedded rays [30]. The results showed that a three-dimensional chain of vortices developed in the wake, agreeing with particle image velocimetry measurements on live fish specimens. Chang *et al.* carried out numerical investigations on a tuna-like swimmer in laminar and turbulent flow regimes [31]. Changes in caudal fin geometry were explored, and it was found that a lunate caudal fin produced less thrust at cruising conditions, but operated at the highest propulsive efficiency. The wake of the tuna-like swimmer was shown to be comprised of a chain of linked vortex rings. Three-dimensional vortex rings have also been observed in the wake of a freely swimming giant danio using synthetic aperture PIV [32]. The effects of aspect ratio on the performance of ellipsoidal flapping foils was modeled by Dong *et al.* [33], who found that maximum propulsive efficiency increases with AR and that thrust coefficient increases monotonically with AR and St. The impact of variations in oscillation frequency, pitching axis location, and the angle of attack of an airfoil on thrust generation were simulated by Sarkar and Venkatraman [34].

In the current work, results obtained from stereoscopic PIV are used to analyze the wake produced by a rigid, trapezoidal panel pitched about its leading edge. The trapezoidal panel geometry was chosen as a rudimentary model for the caudal fin of a variety of fish species. The evolution of wake structures with respect to changes in Strouhal number across the range $0.17 \leq St \leq 0.56$ are

analyzed. The range of tested Strouhal numbers was chosen to match the measured swimming parameters of certain aquatic animals [5]. The current work expands upon the results of Green *et al.*, the earlier work that provided a phase-averaged volume of data at only $St = 0.17$ and 0.28 using planes of two-component PIV that yielded two components of velocity, and only spanwise vorticity. This current work uses stereoscopic PIV to incorporate the third component of velocity, and more importantly all three components of vorticity, into the wake analysis.

II. EXPERIMENTAL SETUP

All experiments were conducted in a recirculating water tunnel located at the Syracuse Center of Excellence. The test section of the tunnel had dimensions of 0.60 m $\times$ 0.60 m $\times$ 2.44 m. The free surface of the test section was enclosed by an acrylic cover to ensure that surface effects were minimized. Upstream of the test section, a honeycomb flow straightener and three screens were used to condition the flow. Two 12-bit Nikon HiSense MKI CCD cameras, each operated with a resolution of 1280 $\times$ 1024 pixels, were mounted above the test section in an angular displacement stereoscopic PIV arrangement. A New Wave Gemini 200-15 Nd-YAG pulsed laser was used to illuminate the wake in a plane at a desired spanwise location. A schematic of the water tunnel test section, laser, and camera setup can be seen in Fig. 1. In the coordinate system of Fig. 1, the positive x-axis is oriented downstream, the y-axis lies along the transverse direction, and the positive z-axis extends vertically, along the span of the panel.

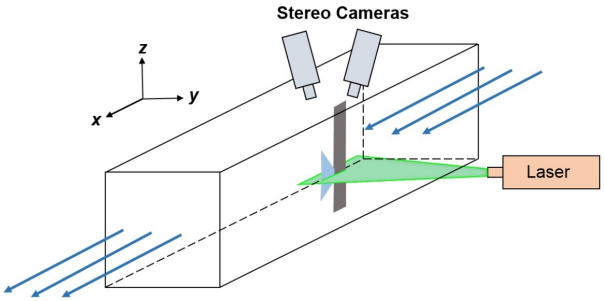

FIG. 1. Water tunnel test section and stereoscopic PIV setup with coordinate axis definitions. Orientation of panel and NACA-0012 fairing are also shown.

The trapezoidal geometry of the panel was chosen as an approximation of a generic caudal fin shape found in a variety of fish species. The panel was made of rigid acrylic that was 1.59 mm thick. The span at the trailing edge, b, was 254 mm, the chord length at the midspan, c, was 101 mm, and the sweep angle of the panel edge was 45°. The details of the panel geometry are displayed in Fig. 2. The aspect ratio of the panel was calculated to be $AR = b^2/S \approx 4.17$, where S was the planform area

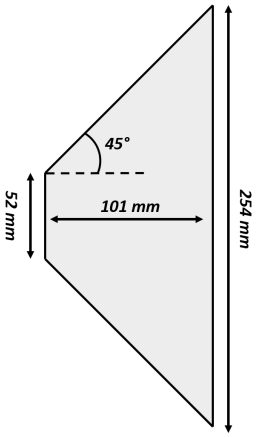

FIG. 2. Geometric details of the trapezoidal pitching panel.

of the panel. The leading edge was attached to a circular pitching shaft of 4.76 mm diameter, and the panel was sinusoidally pitched at a frequency of $f = 1$ Hz with an amplitude of $\pm 7.5°$, which was measured from in-line with the freestream flow. The pitching motion was actuated by a DC motor controlled by a Galil DMC-4123 motion controller. The shaft position was monitored by an optical encoder with a resolution of 1024 counts per revolution. The panel and pitching shaft were mounted behind a stationary fairing with a NACA-0012 cross-section. The trailing edge of the fairing was truncated, giving it a chord length of 50.8 mm, and allowing room for the pitching shaft. The orientation of the panel with respect to the fairing and water tunnel test section can be seen in Fig. 1.

Experiments were conducted at five different freestream speeds, resulting in five combinations of Strouhal and Reynolds numbers. The Reynolds number, Re, was defined as $Re = Uc/\nu$, where ν was the kinematic viscosity of the water. For all five flow speeds, the pitching frequency and pitching amplitude were fixed. A review of the experimental parameters can be found in Table I.

TABLE I. Review of experimental parameters.

U (mm/s)	St	Re (10^3)
156	0.17	15.9
99	0.27	10.2
73	0.37	7.4
57	0.46	5.8
47	0.56	4.8

By mounting the measurement system on a vertically-oriented traverse, PIV images were collected in 29 planes across spanwise extent of the wake. The cameras and laser were mounted on the traverse assembly, and the physical distance between the laser sheet and the cameras

remained constant for all planes of collected data. The PIV planes were spaced 10 mm apart from each other, except for planes at the panel tips and the midspan, which were separated from neighboring planes by 2 mm and 5 mm, respectively. The in-plane spacing between velocity vectors was approximately 2 mm × 2 mm in the x and y directions.

The cameras and laser were operated at 4 Hz, and 19 image pairs were captured at 24 phases of the pitching motion. The resultant velocity vectors were phase-averaged. Camera calibrations were performed for each of the 29 data planes using a pinhole camera model. All PIV images were collected after the first ten pitching cycles in order to eliminate the influence of transient effects on the recorded velocity data. The analysis and collection of PIV images were carried out with Dantec DynamicStudio v3.31 software. Images were evaluated with an adaptive correlation method for an interrogation window of 16 × 16 pixels with 50% overlap in the horizontal and vertical directions. All analysis began with an initial interrogation area window size of 64 × 64 pixels and two refinement steps were used. Polyamid seeding particles with a diameter of approximately 20 μm were used to seed the flow. Particle image diameters were calculated to be approximately 1.2 pixels. For this particle image diameter, simulations show that the RMS random error for cross-correlation digital PIV using a 16 × 16 pixel interrogation window is approximately 0.07 pixels, resulting in RMS error that was no greater than 2% of the freestream velocity for any flow scenario tested [35]. Since stereoscopic PIV was used, three-component velocity vectors were obtained throughout the field of view.

III. RESULTS

All instantaneous velocity vectors obtained from the 29 planes of PIV data were phase-averaged at 24 phases of the pitching motion. The phase-averaged velocity vectors were then interpolated using a cubic spline function. The interpolation produced three-component velocity vectors with a spatial resolution between neighboring vectors of approximately 2 mm × 2 mm × 2.5 mm in the x, y, and z directions, respectively. It is important to note that any flow pattern or structure smaller than the order of the grid spacing of the PIV data ($\approx 0.025c$ in the x and y directions and $\approx 0.1c$ in the z direction) was not captured by the PIV data or the results of the interpolation.

An isometric view of the wake as visualized using isosurfaces of Q-criterion, or simply Q, at two phases of motion for all five Strouhal numbers is shown in Fig. 3. Q is an Eulerian analysis tool that was introduced by Hunt *et al.* that is useful for vortex identification [36]. The local value of Q is calculated from the Frobenius norms of both the rate-of-rotation tensor and the rate-of-strain tensor. Q is defined according to Eqn. 1.

$$Q = \frac{1}{2}(||\mathbf{\Omega}||^2 - ||\mathbf{S}||^2) \tag{1}$$

Here, $\mathbf{\Omega}$ is the rate-of-rotation tensor and $\boldsymbol{S}$ is the rate-of-strain tensor. According to the definition of the Q-criterion, a vortex exists in regions where $Q > 0$, i.e. in a region where $\mathbf{\Omega}$ dominates $\boldsymbol{S}$.

In Figs. 3-6, isosurfaces of Q are plotted at values of 1% of Q_{max}, which is the maximum value of Q as determined from the interpolated, phase-averaged velocity vectors. The value of Q_{max} is a global maximum that was derived from a comparison of all Q values calculated at all phases of motion across all St. The use of 1% of Q_{max} as the isosurface level was chosen for visual clarity of the relevant wake structures. A larger isosurface value would display isosurfaces of larger vorticity magnitude, causing the isosurfaces of Figs. 3-6 to shrink in size and disappear in some places. A lower isosurface value would display isosurfaces of lower vorticity magnitude, causing the isosurfaces of Figs. 3-6 to increase in size, potentially occluding details of vortex shape and evolution.

In Figs. 3-7, the panel and a portion of the wake structures are shown for all five St at two times during the motion of the panel. At $t/T = 0$ (left column of Figs. 3-7), where T is the pitching period, the panel is aligned with the freestream flow and is pitching into the page with maximum angular speed. At $t/T = 0.25$ (right column of Figs. 3-7), the panel is at a motion extreme, moving at zero velocity as it prepares to change direction and begins to pitch out of the page. The wake structures of Figs. 3-7 are shown at these two times in order to display the wake when the panel is pitching at minimum and maximum angular speeds. Although not shown here, the wakes of $t/T = 0.5$ and $t/T = 0.75$ are essentially mirrored versions of the wake at $t/T = 0$ and $t/T = 0.25$, respectively. The isosurfaces of Q shown in Figs. 3-6 are colored from blue to red by the local value of the spanwise vorticity, ω_z, on the isosurface. This coloring scheme allows for a clear visualization of how the components of vorticity are distributed across certain wake structures. Regions of the wake marked by blue or red colors correspond to areas where ω_z is the dominant component of vorticity. In regions of yellow or green color, the prevailing vorticity component is typically the streamwise component, ω_x.

In each half period of the pitching cycle, a spanwise-oriented vortex is shed from the trailing edge, consistent with the development of a 2S wake. In a 2S wake, two single vortices are shed during one pitching cycle. In the current work, the vortices shed from the trailing edge are alternately-signed spanwise vortices arranged to form a reverse von Kármán street. The formation of a reverse von Kármán street is illustrated in Fig. 7, which displays the behavior of ω_z in the midspan plane for all five St at $t/T = 0$ and $t/T = 0.25$. The plots of ω_z in Fig. 7 have been thresholded to only display regions in the midspan plane where $|\omega_z| \geq 5\ s^{-1}$. Due to the imposed variation in the freestream speed among St, the wakes shown

in Figs. 3-7 (and in similar figures) capture information about differing numbers of pitching cycles. Larger St have lower freestream speeds, meaning that vortices are spaced more closely together. Therefore, the vortices generated by a greater number of pitching cycles are still visible in a snapshot of the wake when compared to the wake of a lower St. In addition to the spanwise-oriented vortices generated at the trailing edge, tip vortices are created near the spanwise extremes of the panel. The tip vortices are composed mainly of alternately-signed streamwise vorticity, and they connect with neighboring spanwise vortices, forming an intricate chain of vortex rings. Figures 3-4 show that the wake structures are approximately symmetric about $z/b = 0$. Buchholz *et al.* theorized that the wake of a rectangular pitching panel was composed of a similar series of alternating vortices, that were referred to as horseshoe vortices [22].

The overall wake structure and behavior are dependent on St, as Figs. 3-7 show. However, regardless of the St, the prevailing arrangement of vorticity in at least some portion of the wake assumes the form of a reverse von Kármán street in a region near $z/b \approx 0$ and a chain of rings with alternating rotational sense. The structure of these rings and a reverse von Kármán street near the plane of the midspan are most recognizable when $0.17 \leq St \leq 0.37$. These fundamental wake features becomes increasingly disorganized when $St \geq 0.46$.

A. Spanwise compression and wake breakdown

The wake structures visualized in Fig. 3 are also presented from a side view in Fig. 4. As in Fig. 3, the Q isosurfaces have a value of 1% of Q_{max} and the isosurfaces are colored by spanwise vorticity. A side view of the wake demonstrates that as wake structures convect downstream, they appear to shrink along their spanwise axis, a phenomenon that will be referred to as spanwise compression. Significant spanwise compression is noticeable in Fig. 4 at all St except for $St = 0.17$, which is shown in Figs. 4(a)-(b). When $St = 0.17$, the spanwise-oriented vortices extend across the entire vertical extent of the data window, remaining essentially uncompressed as they convect downstream.

When St is increased, wake compression becomes more exaggerated, as evidenced by the wakes of $0.27 \leq St \leq 0.56$, which are shown in Figs. 4(c)-(j). When $St = 0.27$, the Q isosurfaces extend from $z/b \approx \pm 0.375$ at $x/c \approx 1.0$, and from $z/b \approx \pm 0.3$ at $x/c \approx 1.0$ when $St = 0.37$. Further compression occurs when $St = 0.46$, where the wake stretches from $z/b \approx \pm 0.25$ at $x/c \approx 1.0$. Ultimately, the wake spans from $z/b \approx \pm 0.2$ at $x/c \approx 1.0$ when $St = 0.56$. This trend of greater spanwise compression occurring with increases in St has also been observed in experiments on the wakes generated by trapezoidal and rectangular pitching panels [15, 22]. The relationship among St, streamwise location, and the spanwise extent of the wake in the current work are summarized in Table II. The results shown in Table II report the spanwise extent of the Q isosurfaces in Fig. 4 at $t/T = 0$ in terms of a z/b range at a given streamwise location.

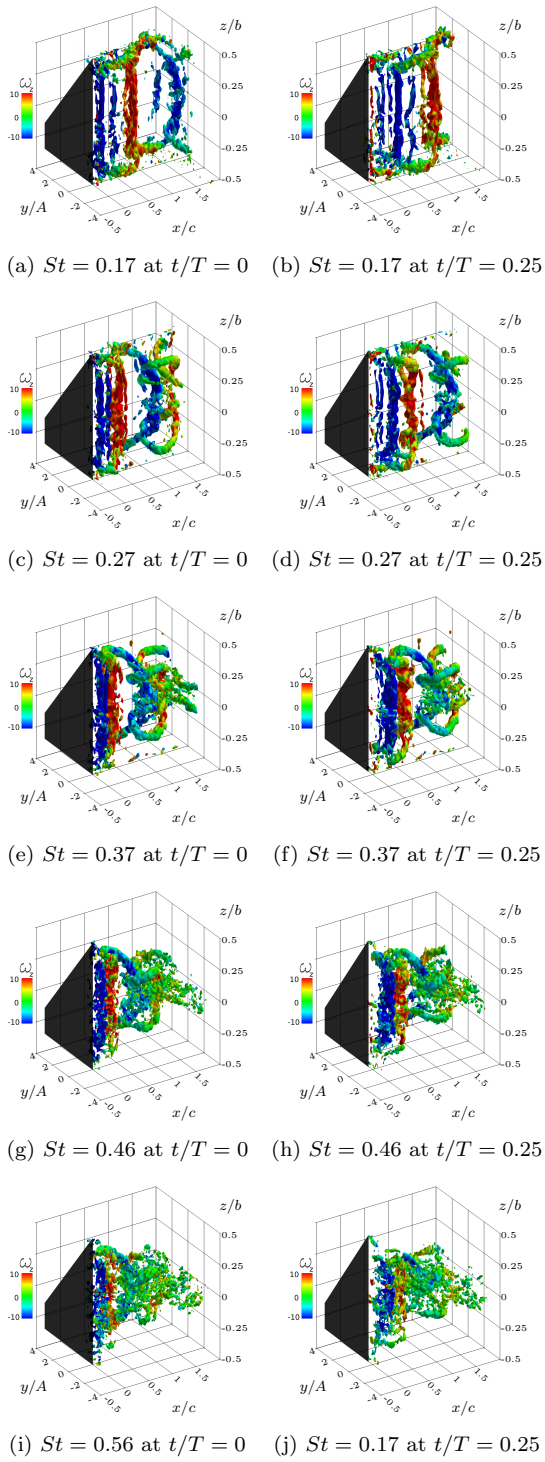

(a) $St = 0.17$ at $t/T = 0$ (b) $St = 0.17$ at $t/T = 0.25$

(c) $St = 0.27$ at $t/T = 0$ (d) $St = 0.27$ at $t/T = 0.25$

(e) $St = 0.37$ at $t/T = 0$ (f) $St = 0.37$ at $t/T = 0.25$

(g) $St = 0.46$ at $t/T = 0$ (h) $St = 0.46$ at $t/T = 0.25$

(i) $St = 0.56$ at $t/T = 0$ (j) $St = 0.17$ at $t/T = 0.25$

FIG. 3. Isometric views of Q isosurfaces at a value of 1% Q_{max} at $t/T = 0$ (left column) and $t/T = 0.25$ (right column) for all five St. Q isosurfaces are colored by the local value of ω_z.

Another characteristic wake behavior that can be ob-

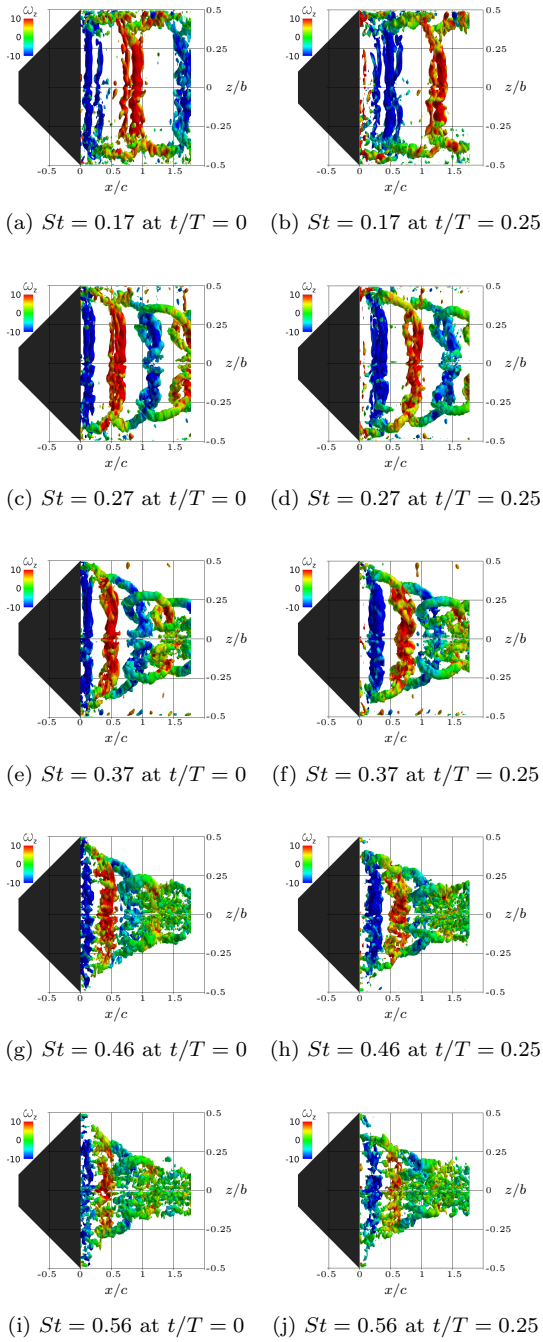

(a) $St = 0.17$ at $t/T = 0$ (b) $St = 0.17$ at $t/T = 0.25$

(c) $St = 0.27$ at $t/T = 0$ (d) $St = 0.27$ at $t/T = 0.25$

(e) $St = 0.37$ at $t/T = 0$ (f) $St = 0.37$ at $t/T = 0.25$

(g) $St = 0.46$ at $t/T = 0$ (h) $St = 0.46$ at $t/T = 0.25$

(i) $St = 0.56$ at $t/T = 0$ (j) $St = 0.56$ at $t/T = 0.25$

FIG. 4. Side views of Q isosurfaces at a level of 1% Q_{max} at $t/T = 0$ (left column) and $t/T = 0.25$ (right column) for all five St. Q isosurfaces are colored by the local value of ω_z.

served in Fig. 4 is a general loss of coherence in wake structures as they convect downstream, a phenomenon that will be referred to as wake breakdown. Wake breakdown manifests itself as a dissolution of organization in the wake, e.g. the disintegration of spanwise vortices and the bending and tearing apart of vortex rings. Similar to spanwise compression, recognizable wake breakdown is not observed when $St = 0.17$ within the data window

TABLE II. Review of spanwise extent of wake structures for all five St at three downstream locations when $t/T = 0$. The spanwise extent of the wake is given in terms of z/b, as estimated from Fig. 4.

St	$x/c = 0.5$	$x/c = 1.0$	$x/c = 1.5$
0.17	$z/b \approx \pm 0.5$	$z/b \approx \pm 0.5$	$z/b \approx \pm 0.5$
0.27	$z/b \approx \pm 0.45$	$z/b \approx \pm 0.375$	$z/b \approx \pm 0.3$
0.37	$z/b \approx \pm 0.4$	$z/b \approx \pm 0.3$	$z/b \approx \pm 0.25$
0.46	$z/b \approx \pm 0.35$	$z/b \approx \pm 0.25$	$z/b \approx \pm 0.2$
0.56	$z/b \approx \pm 0.3$	$z/b \approx \pm 0.2$	$z/b \approx \pm 0.15$

of Figs. 3-4. However, the authors expect wake breakdown to take place beyond the downstream edge of the data window. When $St = 0.27$, wake breakdown begins near the midspan plane at a location of $x/c \approx 1.75$, as shown in Figs. 4(c)-(d). The onset of wake breakdown is recognized by the fact that the spanwise vortices near $x/c \approx 1.75$, visualized through the use of Q isosurfaces, dissolve near the plane of the midspan as the isosurfaces lose spanwise vorticity, indicating a decrease in the organization of wake structures. This loss of spanwise vorticity near the midspan of the wake can also be seen in Fig. 7. The dissolution of spanwise vortices near the plane of the midspan is accompanied by the appearance of streamwise and transverse vorticity, i.e. a region on a Q isosurface colored in green or yellow that had previously been colored in blue or red. Similar wake breakdown behavior is observed in Figs. 4(e)-(j) for $0.37 \leq St \leq 0.56$ near the plane of the midspan, and it then spreads away from the midspan as spanwise structures are destroyed and the wake devolves into a jumbled region of near-zero spanwise vorticity. In certain scenarios, it is also possible to observe a discontinuity in the Q isosurfaces that exist near the plane of the midspan, i.e. spanwise oriented structures do not extend all the way to $z/b \approx 0$. A zoom-in of the region near the plane of the midspan where wake breakdown occurs for $St = 0.27$ and $St = 0.37$ is shown in Fig. 5. The views of the wake presented in Fig. 5 illustrate the dissolution of spanwise vorticity and the tearing apart of spanwise oriented structures during wake breakdown.

With increases in St, the streamwise location corresponding to the onset of wake breakdown moves upstream, towards the trailing edge. Wake breakdown is a phenomenon that typically occurs over some extended portion of the wake; so, the previous and ensuing statements refer mainly to the streamwise location where wake breakdown is first observable from the behavior of Q isosurfaces. When $St = 0.17$, wake breakdown likely occurs beyond the downstream extent of the data window. Wake breakdown behavior is seen at $x/c \approx 1.75$ when $St = 0.27$. Further increases in St lead to wake breakdown beginning to occur at $x/c \approx 1.5$, 1.0, and 0.75 for $St = 0.37$, 0.46, and 0.56, respectively. The locations

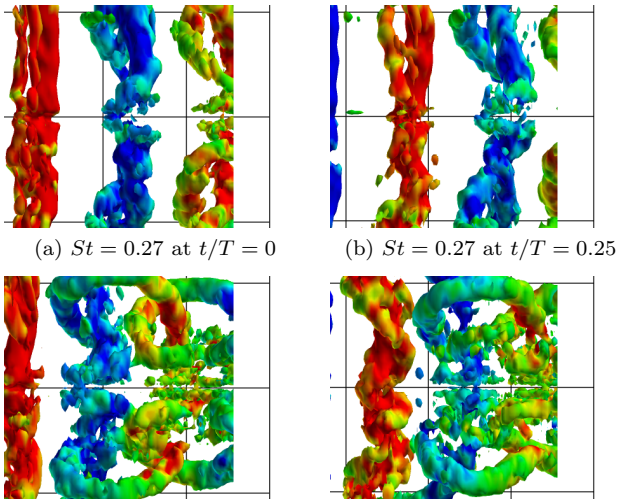

(a) $St = 0.27$ at $t/T = 0$ (b) $St = 0.27$ at $t/T = 0.25$

(c) $St = 0.37$ at $t/T = 0$ (d) $St = 0.37$ at $t/T = 0.25$

FIG. 5. Zoom-in of side views of Q isosurfaces at a level of 1% Q_{max} at $t/T = 0$ (left column) and $t/T = 0.25$ (right column) for $St = 0.27$ and $St = 0.37$. Isosurfaces of Q are colored by the local value of ω_z in the same manner as Fig. 4.

of the onset of wake breakdown, x_{break}, for all five St when $t/T = 0$ are presented in Table III. The values of x_{break} are non-dimensional, and given in terms of an x/c location. These values are estimated from the behavior of the Q isosurfaces of Fig. 4. This trend of the wake breakdown onset location moving upstream with increases in St was previously observed in experiments on the wake produced by a trapezoidal pitching panel by Green *et al.* [15]. In that work, wake breakdown was visualized with isosurfaces of only the out-of-plane vorticity component, ω_z, which was calculated from the results of two-component PIV. Other methods besides the visualization of Q or ω_z isosurfaces have been used to determine the location of wake breakdown [37]. In the current data set, preliminary analysis using the Lagrangian saddles of the finite-time Lyapunov exponent field as in Huang and Green showed a similar trend in the breakdown location. But, the visual inspection of Q isosurfaces is used here for consistency with the other analyses.

TABLE III. Review of the location of the onset of wake breakdown (x_{break}) for all five St when $t/T = 0$. The location of x_{break} is estimated from Fig. 4.

St	x_{break}
0.17	–
0.27	1.75
0.37	1.5
0.46	1.0
0.56	0.5

The wake as viewed from above is presented in Fig. 6. This top view exhibits transverse expansion of the wake that is not easily depicted in the isometric and side views of Figs. 3-4. Greater amounts of transverse expansion are found to occur when St is increased, and the rate of transverse expansion increases at the location where wake breakdown first occurs. Fig. 6 shows that the transverse expansion of the wake is approximately symmetric about $y/A = 0$.

B. Vortex interactions and vortex-induced flow fields

While convecting downstream, each vortex ring interacts with other rings generated during previous and subsequent pitching periods. The vortex rings bend and deform as they move downstream, behaving in a manner that is consistent with the spanwise compression and transverse expansion of the wake. In particular, the bending of the vortex rings in the transverse direction is consistent with the transverse (y-direction) vortex-ring induced velocity that will be described in more detail in section III B 2. These alternating vortex rings are formed by spanwise vortices, which are connected to each other by streamwise vortices at their spanwise tips. As anticipated from the results of the previous section, the effects of spanwise compression, wake breakdown, and transverse expansion are least visible when $St = 0.17$. At the lowest St, there is little deformation of, and interaction between, vortex rings as they move downstream. This lack of deformation and interaction is due in part to the relatively large streamwise spacing between spanwise vortices. The large streamwise spacing is due to the fact that lowest St has the highest freestream speed; therefore, wake structures are convected at the largest speed while shedding frequency remains constant. In the current work, St was increased by decreasing the freestream speed, leading to a more compact streamwise spacing between certain wake structures at higher St. As St is increased, the impact of vortex ring interactions and vortex-induced flow fields on wake behavior becomes significant, which is demonstrated by the increased deformation, bending, spanwise compression, and transverse expansion of vortex rings.

Particular features of wake structure and dynamics can be characterized by interactions among vortices, vortex rings, and vortex-induced velocities. Vortex-induced flow fields can have components in the spanwise, transverse, and streamwise directions. Alternating sign, spanwise-oriented vortices induce transverse flows through vortex rings, consistent with transverse wake expansion. The spanwise vortices also induce flows in the streamwise direction. Streamwise-oriented portions of the vortex rings induce spanwise flow towards the midspan of the wake, consistent with spanwise compression. A general picture of these vortex interactions and vortex-induced velocities for a low St, e.g. $St = 0.17$ or $St = 0.27$, is shown in Fig. 8.

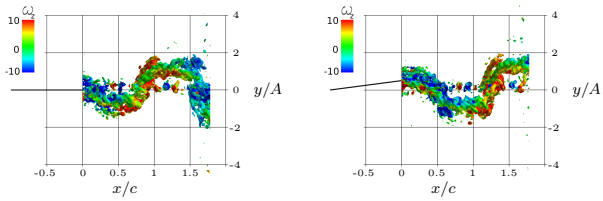

(a) $St = 0.17$ at $t/T = 0$ (b) $St = 0.17$ at $t/T = 0.25$

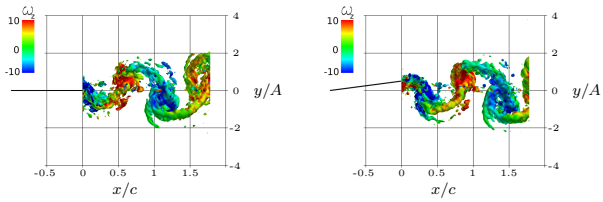

(c) $St = 0.27$ at $t/T = 0$ (d) $St = 0.27$ at $t/T = 0.25$

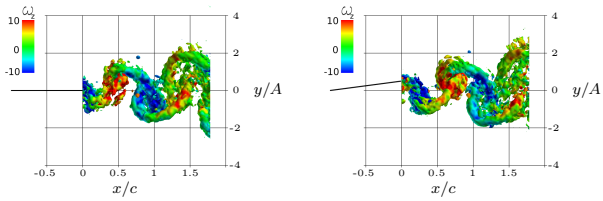

(e) $St = 0.37$ at $t/T = 0$ (f) $St = 0.37$ at $t/T = 0.25$

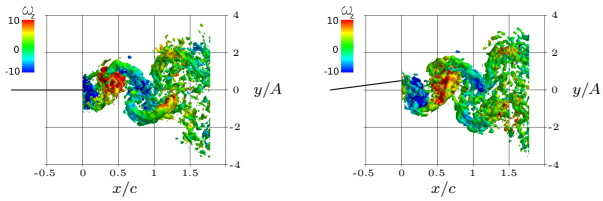

(g) $St = 0.46$ at $t/T = 0$ (h) $St = 0.46$ at $t/T = 0.25$

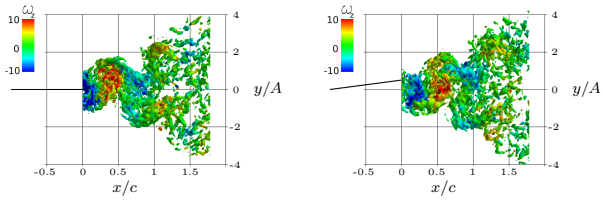

(i) $St = 0.56$ at $t/T = 0$ (j) $St = 0.56$ at $t/T = 0.25$

FIG. 6. Top views of Q isosurfaces at a level of 1% Q_{max} at $t/T = 0$ (left column) and $t/T = 0.25$ (right column) for all five St. Q isosurfaces are colored by the local value of ω_z.

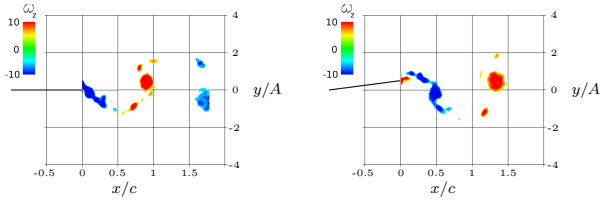

(a) $St = 0.17$ at $t/T = 0$ (b) $St = 0.17$ at $t/T = 0.25$

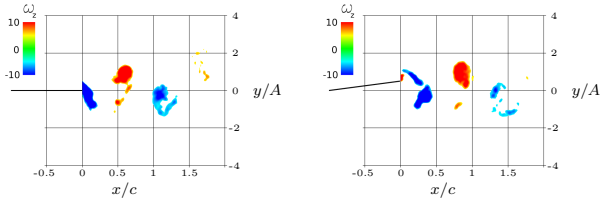

(c) $St = 0.27$ at $t/T = 0$ (d) $St = 0.27$ at $t/T = 0.25$

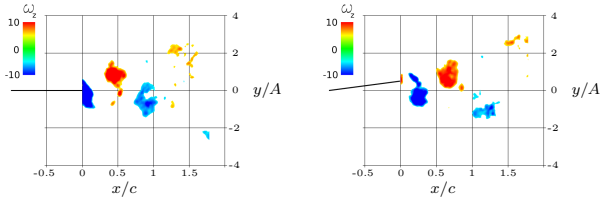

(e) $St = 0.37$ at $t/T = 0$ (f) $St = 0.37$ at $t/T = 0.25$

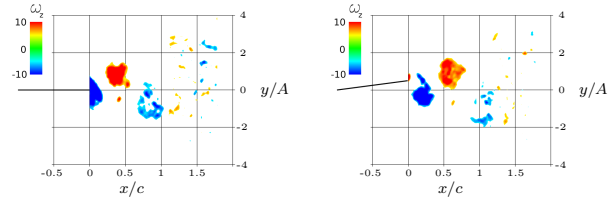

(g) $St = 0.46$ at $t/T = 0$ (h) $St = 0.46$ at $t/T = 0.25$

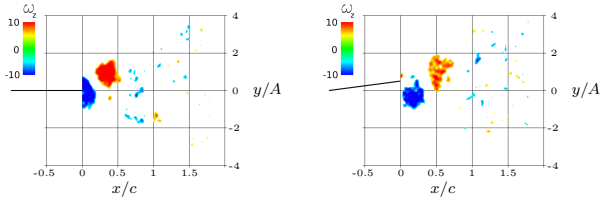

(i) $St = 0.56$ at $t/T = 0$ (j) $St = 0.56$ at $t/T = 0.25$

FIG. 7. Top views of ω_z in the plane of the midspan at $t/T = 0$ (left column) and $t/T = 0.25$ (right column) for all five St. The plots have been thresholded in order to only display regions of the wake where $|\omega_z| \geq 5\ s^{-1}$.

A schematic of the wake for a low St is given in Fig. 8(a), which illustrates the behaviors and effects of alternating vortex rings in the wake. The details of the schematic were developed from the PIV results of $St = 0.27$, which are shown in Fig. 8(b)-(c). Spanwise vortices are shed from the trailing edge and act to induce flow in the transverse and streamwise directions in accor-

dance with their sense of rotation. The development of transverse flows is consistent with transverse wake expansion. Flow is also induced in streamwise directions by the spanwise vortices, but this behavior is not clearly depicted in Fig. 8(a). A shear layer develops along the swept edges of the panel and then rolls up into streamwise vortices that are shed near the spanwise tips of the panel. Regions of upwash and downwash are created by the streamwise vortices, and spanwise flow near the wake centerline moves towards the plane of the midspan, consistent with spanwise compression. It must be noted that the general picture of the wake presented in Fig. 8(a) is no longer valid for $St \geq 0.37$. Figure 8(a) does not include the increased spanwise compression, transverse expansion, and wake breakdown that become more evident when $St \geq 0.37$.

Results obtained from PIV data for $St = 0.27$ are displayed in Figs. 8(b)-(c) to further explain the general wake features shown in Fig. 8(a). In Fig. 8(b), isosurfaces of positive (red) and negative (blue) spanwise vorticity, ω_x, are plotted alongside isosurfaces of positive (gray) and negative (black) spanwise flow, w. The isosurfaces of ω_x have been trimmed in order to isolate the individual streamwise vortices that are found near the spanwise edges of the wake. Similarly, the isosurfaces of w have been restricted to regions in the wake interior, i.e. $-2 \lesssim y/A \lesssim 2$, where flow moves towards the plane of the midspan. Flow is swept around the streamwise vortices, resulting in spanwise flows that move towards the midspan. Figure 8(b) also shows that concentrated regions of spanwise flow are found to coincide with the cores of spanwise vortices at lower St.

Isosurfaces of positive (red) and negative (blue) spanwise vorticity, ω_z, are plotted alongside positive (gray) and negative (black) isosurfaces of transverse flow, v, in Fig. 8(c). The isosurfaces of ω_z have been trimmed in order to isolate four individual spanwise vortices, and the isosurfaces of v have been restricted to the regions between these spanwise vortices. The spanwise vortices interact with each other, inducing flow in a transverse direction as determined by their direction of rotation. The behaviors of these transverse flows, as illustrated by the isosurfaces of v, is consistent with transverse wake expansion.

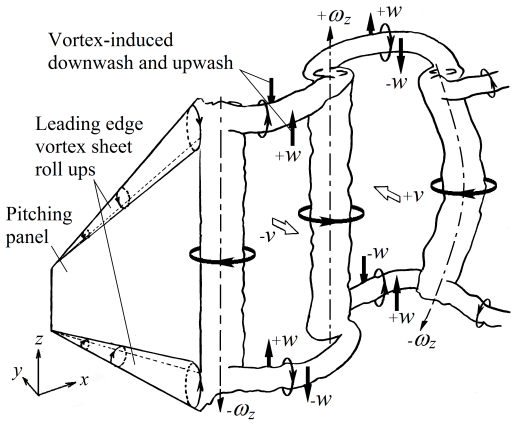

(a) Schematic of general wake features and vortex-induced flow fields at a low St, e.g. $St = 0.17$ or $St = 0.27$

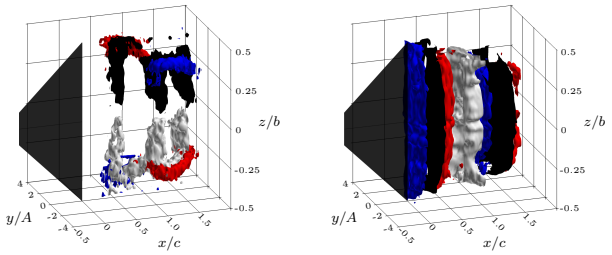

(b) Isosurfaces of $\omega_x = \pm 10$ s^{-1} (red/blue) and $w = \pm 40$ mm/s (gray/black)

(c) Isosurfaces of $\omega_z = \pm 10$ s^{-1} (red/blue) and $v = \pm 20$ mm/s (gray/black)

FIG. 8. Schematic of general wake features and vortex-induced flow fields, and isosurfaces obtained from PIV data. Isosurfaces of ω_x, ω_z, v, and w are shown for $St = 0.27$ at $t/T = 0$.

1. *Vortex-induced spanwise velocity*

Isosurfaces of spanwise velocity, w, at $t/T = 0$ and $t/T = 0.25$ for all five St are shown from a side view in Fig. 9 and a top view in Fig. 10. Isosurfaces of w plotted at a value of 25 mm/s are shown in gray, while isosurfaces of w plotted at a value of -25 mm/s are shown in black. Note that the isosurfaces of Figs. 9-8 are plotted at a lower magnitude of w than those in Fig. 8(b). The lower magnitude isosurfaces allow for better visualization of the spanwise flows that move away from the midspan, which occur along the transverse edges of the wake. When $0.17 \leq St \leq 0.27$, spanwise flow exists in the cores of the spanwise vortices, where the flow is oriented towards the midspan plane of the wake. The presence of axial flow in the cores of spanwise vortices was also observed by Koochesfahani *et al.* using flow visualization in the wake of an oscillating airfoil [9]. The connection between spanwise flow and spanwise vortices when $St = 0.17$ is made apparent by comparing the isosurfaces of w in Figs. 9(a)-(b) with the Q isosurfaces in Figs. 4(a)-(b). The spanwise vortex cores, inferred from the Q isosurfaces, are co-located with the isosurfaces of w near $x/c \approx 1$ and $x/c \approx 1.75$ for $t/T = 0$, and near $x/c \approx 0.5$ and $x/c \approx 1.25$ for $t/T = 0.25$. The relationship between spanwise flow and the location of spanwise vortices is also seen when $St = 0.27$. Three distinct regions of large magnitude spanwise flow can be observed in Figs. 9(c)-(d). The locations of these three regions align well with the positions of the three spanwise vortices shown in Figs. 4(c)-(d). Prior to the onset of wake breakdown, there is still a connection between spanwise flow and spanwise vortex cores when $St = 0.37$. Figures 9(e)-(f) demonstrate that a concentrated region of flow towards the midspan plane exists at $x/c \approx 0.5$, agree-

ing with the positions of spanwise vortices observed in Figs. 4(e)-(f). Also note that when $0.17 \leq St \leq 0.37$, spanwise flows develop near the trailing edge, in accordance with the nascent spanwise vortices found immediately downstream of the trailing edge in Figs. 4(a)-(f). The relationship between spanwise flow and the cores of spanwise vortices is less clear when $St \geq 0.46$, as the wake in general loses coherence and organization.

Spanwise velocity near the plane of the midspan ($z/b = 0$) is shown to be negligible when St is low. This is demonstrated by the isosurfaces of w in Figs. 9(a)-(b), and to a lesser degree, by the isosurfaces shown in Figs. 9(c)-(d). This demonstration of negligible spanwise flow near $z/b = 0$ at low St agrees well with a minimal spanwise flow assumption by Green *et al.* that was necessary for a 2D Lagrangian wake analysis on the wake produced by a trapezoidal panel [15, 37]. This assumption breaks down at larger St, as shown by Figs. 9(e)-(j).

A top view of the wake indicates that small regions of spanwise flow develop along the transverse edges of the streamwise vortex segments, which is apparent in Fig. 10. Areas of flow away from the midspan are found along the exterior of the wake, surrounding the flow towards the midspan that exists in the interior of the wake, a trait that occurs across all St. For all St, the isosurfaces of flow towards the midspan are larger than those for flow away from the midspan. The shapes and distributions of the w isosurfaces of Fig. 10 follow the general trends of transverse wake expansion, i.e. increases in St produce greater transverse wake expansion. The development of spanwise flow away from the midspan, along the exterior of the wake, is related to the presence and orientation of streamwise vortices. These vortices originate near the spanwise tips of the panel, and the flows that they induce are consistent with spanwise wake compression.

The relationship between streamwise vorticity and spanwise flow at low St was first introduced in Fig. 8, and is detailed further for all five St by Fig. 11. Isosurfaces of streamwise vorticity (ω_x), rather than Q, are displayed alongside isosurfaces of spanwise velocity (w) at a time of $t/T = 0$ in Fig. 11. Red and blue isosurfaces of ω_x, are plotted at a value of $\pm$ 10 s^{-1}, while gray and black isosurfaces of w are plotted at a value of $\pm$ 40 mm/s. In order to better visualize the connections between ω_x and w, Fig. 11 uses a higher magnitude of w for the isosurfaces than those displayed in Figs. 9-10. Although isosurfaces of ω_x are found throughout the wake in Fig. 11, those that lie along the spanwise edges of the wake are the most important when it comes to a discussion of spanwise wake compression.

In general, flow is swept around the streamwise vortices, ultimately moving along the center of the wake towards the midspan plane, consistent with spanwise compression. This interaction between vorticity and spanwise flows becomes demonstrable at $St = 0.27$, as displayed in Figs. 11(c)-(d). By using the right hand rule, one can see that the streamwise vortices at the spanwise edges of the wake, regardless of their sense of rotation, induce flow away from the midspan, along the transverse exterior of the wake. As this flow is swept around a streamwise vortex, it moves towards the midspan plane, leading to a region of spanwise flow such as the black isosurfaces of $-w$

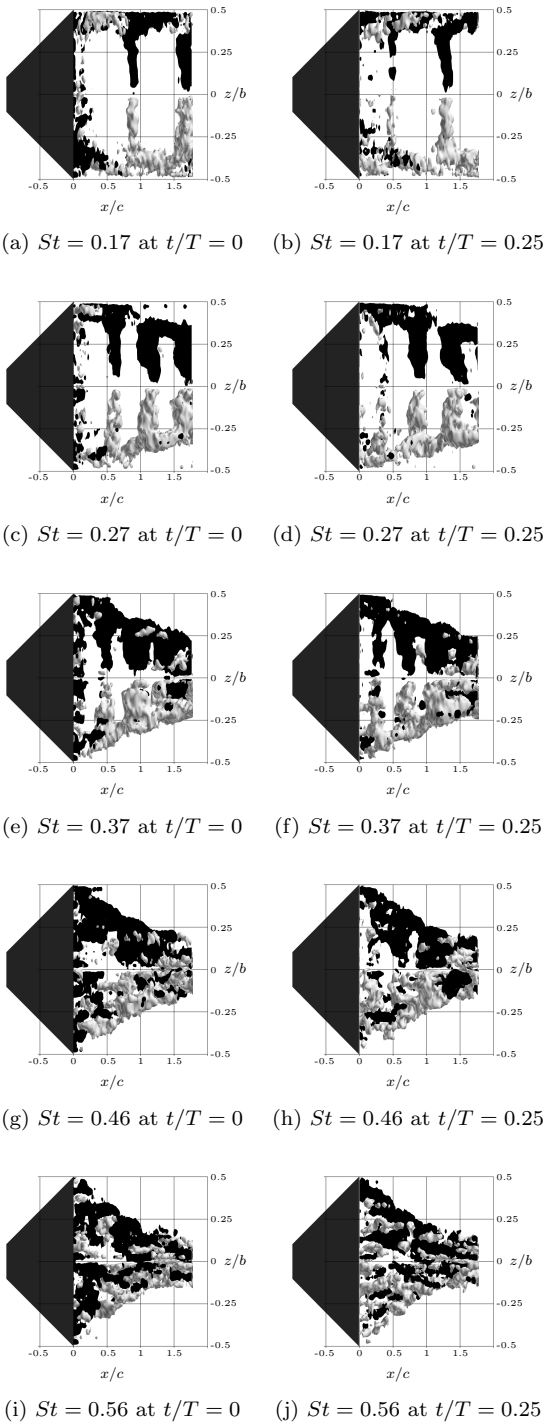

(a) $St = 0.17$ at $t/T = 0$ (b) $St = 0.17$ at $t/T = 0.25$

(c) $St = 0.27$ at $t/T = 0$ (d) $St = 0.27$ at $t/T = 0.25$

(e) $St = 0.37$ at $t/T = 0$ (f) $St = 0.37$ at $t/T = 0.25$

(g) $St = 0.46$ at $t/T = 0$ (h) $St = 0.46$ at $t/T = 0.25$

(i) $St = 0.56$ at $t/T = 0$ (j) $St = 0.56$ at $t/T = 0.25$

FIG. 9. Side views of w isosurfaces at $t/T = 0$ (left column) and $t/T = 0.25$ (right column) for all five St. Gray isosurfaces are presented at $w = 25$ mm/s and black isosurfaces are presented at $w =$ -25 mm/s.

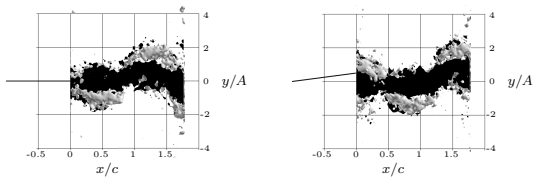

(a) $St = 0.17$ at $t/T = 0$ (b) $St = 0.17$ at $t/T = 0.25$

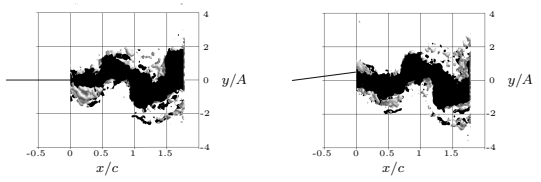

(c) $St = 0.27$ at $t/T = 0$ (d) $St = 0.27$ at $t/T = 0.25$

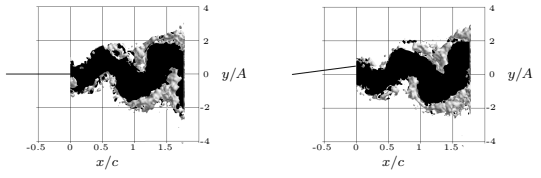

(e) $St = 0.37$ at $t/T = 0$ (f) $St = 0.37$ at $t/T = 0.25$

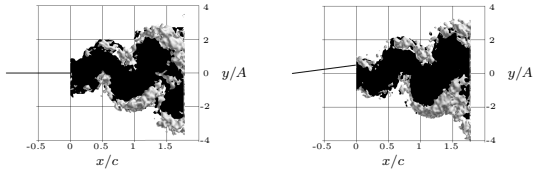

(g) $St = 0.46$ at $t/T = 0$ (h) $St = 0.46$ at $t/T = 0.25$

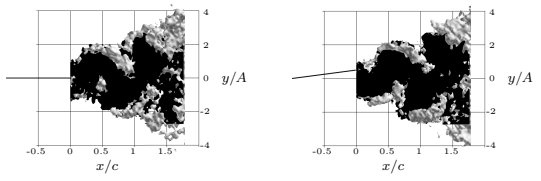

(i) $St = 0.56$ at $t/T = 0$ (j) $St = 0.56$ at $t/T = 0.25$

FIG. 10. Top views of w isosurfaces at $t/T = 0$ (left column) and $t/T = 0.25$ (right column) for all five St. Gray isosurfaces are presented at w = 25 mm/s and black isosurfaces are presented at w = -25 mm/s.

seen in the top views of Fig. 11. Along the interior of the wake, there is a confluence of vortex-induced flows, leading to a large region of flow towards the midspan. Even as the wake experiences spanwise compression, the sweeping up of flow around these streamwise-oriented vortices continues to be evident. A similar analysis can be applied to Figs. 11(e)-(j) in order to describe the causes of spanwise compression at higher St.

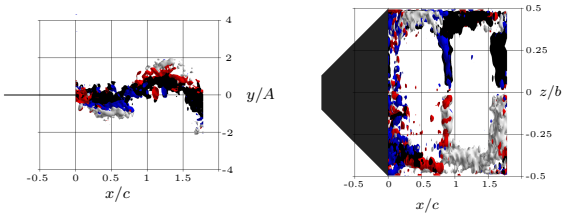

(a) $St = 0.17$ at $t/T = 0$ (b) $St = 0.17$ at $t/T = 0$

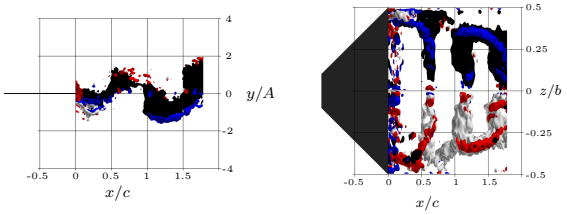

(c) $St = 0.27$ at $t/T = 0$ (d) $St = 0.27$ at $t/T = 0$

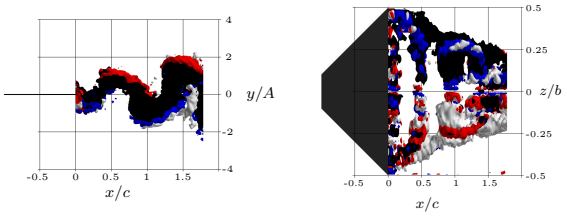

(e) $St = 0.37$ at $t/T = 0$ (f) $St = 0.37$ at $t/T = 0$

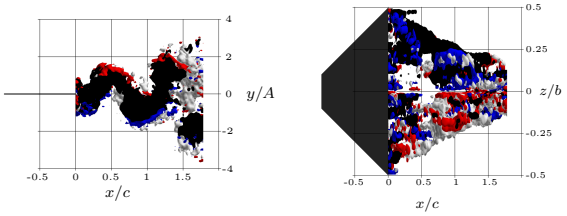

(g) $St = 0.46$ at $t/T = 0$ (h) $St = 0.46$ at $t/T = 0$

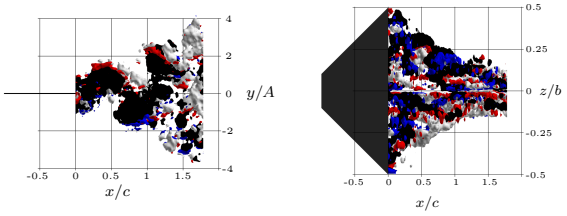

(i) $St = 0.56$ at $t/T = 0$ (j) $St = 0.56$ at $t/T = 0$

FIG. 11. Top views (left column) and side views (right column) of isosurfaces of ω_x and w at $t/T = 0$ (left column) for all five St. Red and blue isosurfaces of ω_x are presented at $\omega_x = 10\ s^{-1}$ and $\omega_x = -10\ s^{-1}$, respectively. Gray and black isosurfaces of w are presented at w = 40 mm/s and w = -40 mm/s, respectively.

2. Vortex-induced transverse velocity

The transverse velocity, v, also plays an important role in overall wake dynamics. Transverse velocity fields are compared for all five St using isosurfaces of v at times of $t/T = 0$ and $t/T = 0.25$ in Figs. 12-13. A side view of the isosurfaces is shown in Fig. 12 and a top view of the isosurfaces is shown in Fig. 13. Isosurfaces of v that are plotted at a velocity of 20 mm/s are shown in gray, and isosurfaces of v that are plotted at a velocity of -20 mm/s are shown in black. As one would expect from previous discussions, the isosurfaces of v reveal that increases in St are associated with greater spanwise wake compression and transverse wake expansion, as well as the upstream movement of the onset of wake breakdown. The development of transverse flows in the wake is intimately linked to the behavior of vortex rings, as was noted during the previous discussion of Fig. 8(a). It was proposed that transverse flow is induced through the vortex rings in a manner that is consistent with transverse wake expansion, a proposition that is substantiated by Figs. 12-13.

Consider the vortex ring that exists between $1.25 \lesssim x/c \lesssim 2.0$ in Figs. 3-6 for $St = 0.27$ at $t/T = 0$. This ring is composed of a positive spanwise vortex at its downstream end and a negative spanwise vortex at its upstream end. The two spanwise vortices are linked to each other at their spanwise tips by a pair of streamwise vortices. Using the right hand rule, one can see that transverse flow will be induced between the spanwise vortices in the $-y$ direction. Transverse flows will be induced by the actions of both the spanwise and streamwise vortices. The induced flow of this vortex ring in the $-y$ direction is consistent with the transverse offset of this ring as seen in Fig. 6(c). By similar reasoning, the vortex ring found in Fig. 4(c) that exists between $0.5 \lesssim x/c \lesssim 1.25$ would have a self-induced velocity in the $+y$ direction. Figure 6(c) shows that at least some part of this vortex ring moves in that transverse direction. Note that the transverse expansion mostly effects the streamwise vortices, which bend away from the interior of the wake, while the spanwise vortices remain relatively close to the centerline of the wake. This is due to the fact that each spanwise vortex constitutes a leg of two subsequent vortex rings, each with opposite self-induced velocity. A closer inspection of Figs. 3(c)-(d) shows that each spanwise vortex is in fact two spanwise vortex legs twisted together, with one leg from each vortex ring. As the two vortex rings try to pull apart in opposite direction, the spanwise legs remain near the centerline of the wake.

Comparison of Fig. 4 with Fig. 12 at the same St establishes that alternating vortex rings act to induce transverse velocities that are consistent with transverse wake expansion. When $St = 0.17$, there are two large regions of oppositely-signed v which are associated with the locations of two vortex rings in the wake. Note that the transitions between positive and negative v in Figs. 12(a)-(b) and Figs. 13(a)-(b) occur in the vicinity of the spanwise vortices shown in Figs. 4(a)-(b). The isosurfaces of v are also consistent with the induced flows of the streamwise-oriented segments of the vortex rings. The relationship between transverse flow and vortex rings can

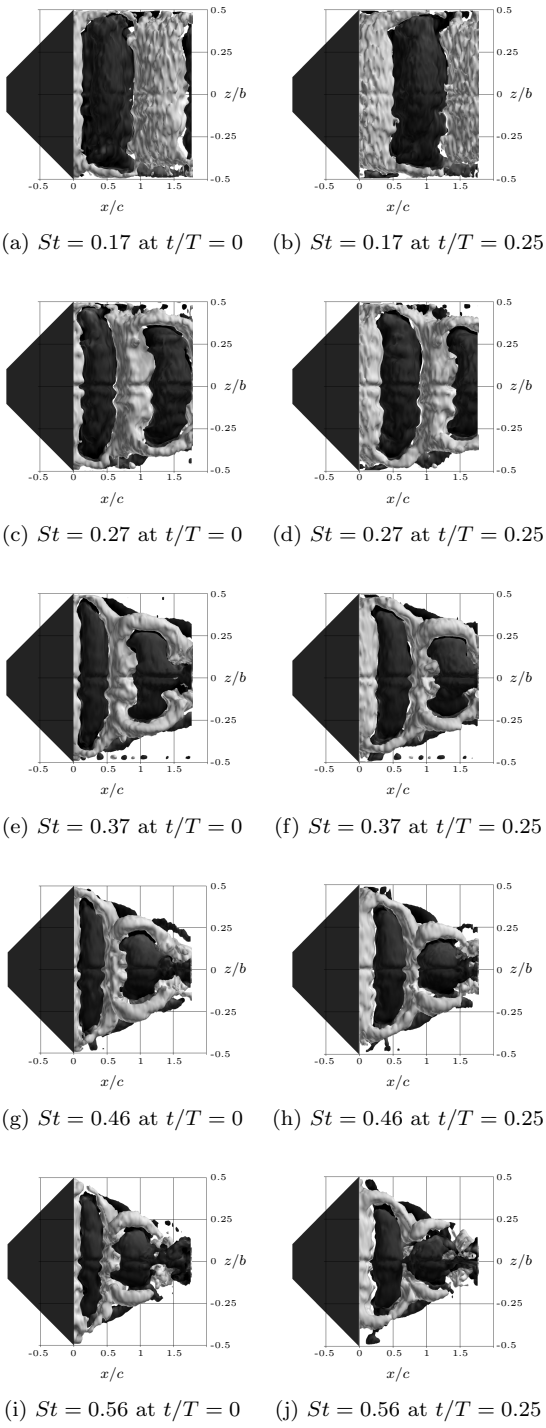

(a) $St = 0.17$ at $t/T = 0$ (b) $St = 0.17$ at $t/T = 0.25$

(c) $St = 0.27$ at $t/T = 0$ (d) $St = 0.27$ at $t/T = 0.25$

(e) $St = 0.37$ at $t/T = 0$ (f) $St = 0.37$ at $t/T = 0.25$

(g) $St = 0.46$ at $t/T = 0$ (h) $St = 0.46$ at $t/T = 0.25$

(i) $St = 0.56$ at $t/T = 0$ (j) $St = 0.56$ at $t/T = 0.25$

FIG. 12. Side views of v isosurfaces at $t/T = 0$ (left column) and $t/T = 0.25$ (right column) for all five St. Gray isosurfaces are presented at $v = 20$ mm/s and black isosurfaces are presented at $v =$ -20 mm/s.

also be observed from the top views of the wake shown in Figs. 13(a)-(b). When $St = 0.27$, the wake consists of three vortex rings, as shown in Fig. 4(c)-(d). The induced flows of the vortex rings are in agreement with the v isosurfaces of Figs. 12(c)-(d) and Figs. 13(c)-(d), where three distinct regions of transverse flow correspond to the locations of three vortex rings.

Regardless of St, a well-defined link is established between the distribution of vortex rings and transverse flow; however, this link disappears in the regions of appreciable wake breakdown that appear at higher St. When $0.37 \leq St \leq 0.56$, wake breakdown behavior is visible in the v isosurfaces that are shown from a side view in Figs. 12(e)-(j). Near the downstream end of the data window, the gray isosurfaces of v do not extend to the plane of the midspan. The phenomenon of wake breakdown begins near the plane of the midspan, and then spreads outwards, tearing apart these v isosurfaces in the process. The top views of the wake as presented in Figs. 13(g)-(j) show that when $0.46 \leq St \leq 0.56$, wake breakdown leads to the disintegration of interconnected loops of v isosurfaces. Downstream of where wake breakdown begins, the transverse flows in the wake become divided into two large regions of opposing flow, away from the centerline of the wake. This is consistent with the bifurcation of wake structures that was described by Kumar *et al.* [38].

3. Vortex-induced streamwise velocity

The interactions between spanwise vortices can induce streamwise flows with velocities that exceed the freestream velocity, consistent with the generation of momentum in the streamwise direction. This addition of streamwise momentum in relation to spanwise vortices is often associated with a reverse von Kármán street and thrust production by pitching foils or panels. The induced streamwise velocity, when non-dimensionalized via a scaling by the freestream speed, has been previously shown to increase monotonically with St for experiments on a trapezoidal pitching panel [38]. The trend of increasing non-dimensional streamwise velocity, i.e. non-dimensional streamwise momentum, was shown to occur in both phase-averaged and time-averaged velocity fields, and the distribution of momentum in the wake was found to be consistent with the organization of vortical structures in the wake and their induced velocities. The wake region downstream of the vortex ring breakdown has been shown to develop a time-averaged velocity profile in the form of a bifurcated jet structure. Furthermore, four distinct jets can emerge in the time-averaged profile if St is large enough. The emergence of four distinct momentum jets in the time-averaged velocity field has been called a "quadfurcated" jet by Van Buren *et al.*[21].

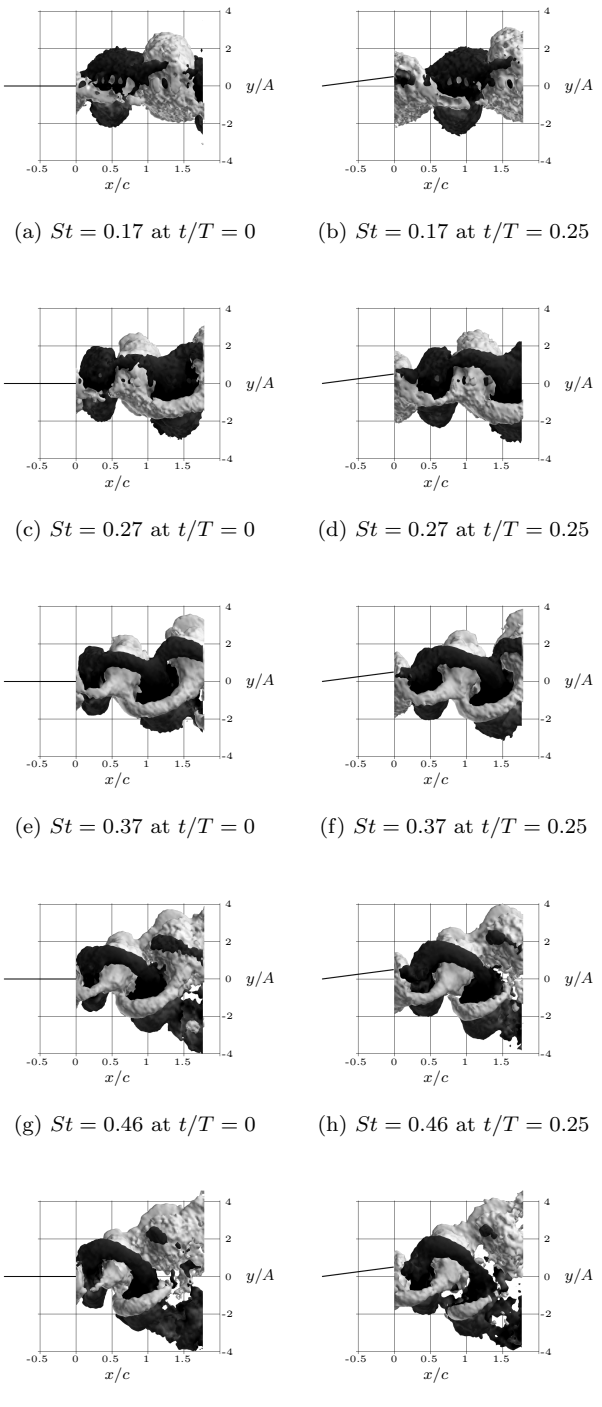

(a) $St = 0.17$ at $t/T = 0$ (b) $St = 0.17$ at $t/T = 0.25$

(c) $St = 0.27$ at $t/T = 0$ (d) $St = 0.27$ at $t/T = 0.25$

(e) $St = 0.37$ at $t/T = 0$ (f) $St = 0.37$ at $t/T = 0.25$

(g) $St = 0.46$ at $t/T = 0$ (h) $St = 0.46$ at $t/T = 0.25$

(i) $St = 0.56$ at $t/T = 0$ (j) $St = 0.56$ at $t/T = 0.25$

FIG. 13. Top views of v isosurfaces at $t/T = 0$ (left column) and $t/T = 0.25$ (right column) for all five St. Gray isosurfaces are presented at v = 20 mm/s and black isosurfaces are presented at v = -20 mm/s.

IV. SUMMARY

The three-dimensional wake behind a low aspect ratio trapezoidal pitching panel has been studied using stereoscopic particle image velocimetry. The evolution of wake structures and wake behavior with respect to changes in Strouhal number over five Strouhal numbers in the range 0.17-0.56 were analyzed. Isosurfaces of the Q criterion, transverse velocity, spanwise velocity, and streamwise vorticity were used to shed light on the relationships between vorticity, velocity, and various wake phenomena.

Spanwise vortices were shown to be shed from the trailing edge of the panel, forming a reverse von Kármán vortex street in the wake. A reverse von Kármán street was detected in at least some sections of the wake at all five Strouhal numbers. Streamwise vortices were created near the spanwise tips of the panel, connecting with spanwise vortices to create vortex rings. A connected chain of vortex rings was shown to exist at each St, prior to the onset of wake breakdown. Wake breakdown was observed to occur when the wake structures began to lose overall coherence and organization, and increases in the Strouhal number were shown to move the location of the onset of wake breakdown upstream. The effects of wake breakdown manifested in the behaviors of isosurfaces of velocity components and of the Q criterion. The induced velocities of the vortex rings were consistent with transverse velocities and transverse expansion of the wake. Increases in Strouhal number were also shown to correspond to a greater amount of transverse wake expansion.

At the spanwise edges of the wake, the dominant component of vorticity was in the streamwise direction. Streamwise vortices were associated with spanwise flow, which moved away from the plane of the midspan at the transverse edges of the wake, and towards the plane of the midspan in the interior of the wake. The confluence of spanwise flow towards the plane of the midspan in the wake interior was consistent with spanwise compression. At lower Strouhal numbers, spanwise flow was found to be concentrated in the cores of spanwise vortices. A final observed effect of increasing Strouhal number was an increase in the rate of spanwise compression of the wake.

ACKNOWLEDGMENTS

This work was supported by the Office of Naval Research under ONR Award No. N00014-14-1-0418.

[1] George V. Lauder and Peter G.A. Madden, "Fish locomotion: kinematics and hydrodynamics of flexible foil-like fins," Exp. Fluids **43**, 641–653 (2007).
[2] M.J. Lighthill, "Hydromechanics of aquatic animal propulsion," Ann. Rev. Fluid Mech. **1**, 413–446 (1969).
[3] J.M. Anderson, K. Streitlein, D.S. Barrett, and M.S. Triantafyllou, "Oscillating foils of high propulsive efficiency," J. Fluid Mech. **360**, 41–72 (1998).
[4] H. Yamaguchi and N. Bose, "Oscillating foils for marine propulsion," in *Proceedings of the Fourth (1994) International Offshore and Polar Engineering Conference*, Vol. 3 (The International Society of Offshore and Polar Engineers, 1994).
[5] G.S. Triantafyllou, M.S. Triantafyllou, and M.A. Grosenbaugh, "Optimal thrust development in oscillating foils with application to fish propulsion," Journal of Fluids and Structures **7**, 205–224 (1993).
[6] Peter Freymuth, "Propulsive vortical signature of plunging and pitching airfoils," AIAA Journal **26**, 881–883 (1988), july.
[7] Peter Freymuth, "Thrust geenration by an airfoil in hover modes," Exp. Fluids **9**, 17–24 (1990).
[8] Knut Streitlien, George S. Triantafyllou, and Michael S. Traintafyllou, "Efficient foil propulsion through vortex control," AIAA Journal **34**, 2315–23119 (1996).
[9] M.M. Koochesfahani, "Vortical patterns in the wake of an oscillating foil," AIAA Journal **27**, 1200–1205 (1989).
[10] L Schouveiler, F.S. Hover, and M.S. Triantafyllou, "Performance of flapping foil propulsion," Journal of Fluids and Structures **20**, 949–959 (2005).
[11] A.W. Mackowski and C.H.K. Williamson, "Direct measurement of thrust and efficiency of an airfoil undergoing pure pitching," J. Fluid Mech. **765**, 524–543 (2015).
[12] Douglas G. Bohl and Manoochehr M. Koochesfahani, "Mtv measurements of the vortical field in the wake of an airfoil oscillating at high reduced frequency," J. Fluid Mech. **620**, 63–88 (2009).
[13] M.S. Triantafyllou, G.S. Triantafyllou, and R. Gopalkrishnan, "Wake mechanics for thrust generation in oscillating foils," Physics of Fluids A: Fluid Dynamics **12**, 2835–2837 (1991).
[14] C.H.K Williamson and A. Roshko, "Vortex formation in the wake of an oscillating cylinder," Journal of Fluids and Structures **2**, 355–381 (1988).
[15] Melissa A. Green, Clarence W. Rowley, and Alexander J. Smits, "The unsteady three-dimensional wake produced by a trapezoidal pitching panel," J. Fluid Mech. **685**, 117–145 (2011).
[16] Kazuo Ohmi, Madeleine Coutanceau, Ta Phuoc Loc, and Annie Dulieu, "Vortex formation around an oscillating and translating airfoil at large incidences," J. Fluid Mech. **211**, 37–60 (1990).
[17] Kazuo Ohmi, Madeleine Coutanceau, Olivier Daube, and Ta Phuoc Loc, "Further experiments on vortex formation around an oscillating and translating airfoil at large incidences," J. Fluid Mech. **225**, 607–630 (1991).
[18] James H.J. Buchholz and Alexander J. Smits, "On the evolution of the wake structure produced by a low-aspect-ratio pitching panel," J. Fluid Mech. **564**, 433–443 (2005).
[19] K.D. von Ellenrieder, K. Parker, and J. Soria, "Flow structures behind a heaving and pitching finite-span wing," J. Fluid Mech. **490**, 129–138 (2003).
[20] James H.J. Buchholz and Alexander J. Smits, "On the

evolution of wake structure produced by a low-aspect-ratio pitching panel," J. Fluid Mech. **546**, 433–443 (2006).

[21] Tyler Van Buren, D. Floryan, D. Brunner, U. Senturk, and Alexander J. Smits, "Impact of trailing edge shape on the wake and propulsive performance of pitching panels," Physical Review Fluids (2017).

[22] James H.J. Buchholz and Alexander J. Smits, "The wake structure and thrust performance of a rigid low-aspect-ratio pitching panel," J. Fluid Mech. **603**, 331–365 (2008).

[23] Kara L. Feilich and George V. Lauder, "Passive mechanical models of fish caudal fins: effects of shape and stiffness on self-propulsion," Bioinspiration & Biomimetics **10** (2015).

[24] Jeongsu Lee, Yong-Jai Park, Kyu-Jin Cho, Daegyoum Kim, and Ho-Young Kim, "Hydrodynamic advantages of a low aspect-ratio flapping foil," Journal of Fluids and Structures **71**, 70–77 (2017).

[25] Daniel B. Quinn, *Optimizing the Efficiency of Batoid-Inspired Swimming*, Ph.D. thesis, Princeton University (2015).

[26] D. Kim and M. Gharib, "Experimental study of three-dimensional vortex structures in translating and rotating plates," Exp. Fluids **49**, 329–339 (2010).

[27] Adam C. DeVoria and Matthew J. Ringuette, "Vortex formation and saturation for low-aspect-ratio rotating flat-plate fins," Exp. Fluids **52**, 441–462 (2012).

[28] Laura Guglielmini, Paolo Blondeaux, and Giovanna Vittori, "A simple model of propulsive oscillating foils," Ocean Engineering **31**, 883–899 (2003).

[29] Paolo Blondeaux, Francesco Fornarelli, Laura Guglielmini, Michael S. Triantafyllou, and Roberto Verzicco, "Numerical experiments on flapping foils mimicking fish-like locomotion," Physics of Fluids **17** (2005).

[30] Q. Zhu and Kourosh Shoele, "Propulsion performance of a skeleton-strengthened fin," The Journal of Experimental Biology **211**, 2087–2100 (2008).

[31] Xinghua Chang, Laiping Zhang, and Xin He, "Numerical study of the thunniform mode of fish swimming with different reynolds number and caudal fin shape," Computers & Fluids **68**, 54–70 (2012).

[32] Leah Mendelson and Alexandra H. Techet, "Quantitative wake analysis of a freely swimming fish using 3d synthetic aperture piv," Experiments in Fluids **56** (2015).

[33] H. Dong, R. Mittal, and F.M. Najjar, "Wake topology and hydrodynamic performance of low-aspect-ratio flapping foils," J. Fluid Mech. **566**, 309–343 (2006).

[34] Sunetra Sarkar and Kartik Venkatraman, "Numerical simulation of thrust generating flow past a pitching airfoil," Computers & Fluids **35**, 16–42 (2006).

[35] Markus Raffel, Christian E. Willert, Steve T. Wereley, and Jurgen Kompenhans, *Particle Image Velocimetry: A Practical Guide* (Springer, 2007).

[36] J.C.R. Hunt, A.A. Wray, and P. Moin, "Eddies, streams, and convergenze zones in turblent flows," Center for Turbulence Research Proceedings of the Summer Program 1988 , 193–202 (1988).

[37] Y. Huang and M.A. Green, "Detection and tracking of vortex phenomena using lagrangin coherent structures," Exp. Fluids **56(147)**, 1–12 (2015).

[38] Rajeev Kumar, Justin T. King, and Melissa A. Green, "Momentum distribution in the wake of a trapezoidal pitching panel," Mar. Technol. Soc. Journal **50(5)**, 9–23 (2016).